

# Splats Formation, Interaction and Residual Stress Evolution in Thermal Spray Coating Using a Hybrid Computational Model

Abba A. Abubakar<sup>1</sup> · Abul Fazal M. Arif<sup>1</sup> · Syed Sohail Akhtar<sup>1</sup> · Javad Mostaghimi<sup>2</sup>

Submitted: 29 June 2018 / in revised form: 21 December 2018 / Published online: 23 January 2019  
© ASM International 2019

**Abstract** Due to the multilayered pattern of coating deposition, residual stresses are commonly developed in thermal spray coatings (TSCs). The large deformation, complex interaction and material mismatch are the main contributing factors to residual stress formation. The constitutive behavior and lifetime are directly dependent on the nature and extent of the residual stress field. In the present study, a computational approach for effective prediction of residual stress evolution in TSCs has been proposed. The proposed approach is hybrid in the sense that it combines “point cloud” (PC) and finite elements (FE) to model the residual stresses. Sprayed droplets deposition and associated deformations are captured on PC using smooth particle hydrodynamics, a popular meshless approach for modeling of violent fluid flows. The conversion of deformed droplets from PC to FE domains is done using several recent algorithms for point cloud processing. Then, conventional FE schemes are used to model the heat transfer and structural deformation occurring during the process. The proposed approach has been found to be effective in predicting residual stress evolution in thermal barrier coatings (TBCs). It can capture the effects of microstructural defects (such as pores and cracks) and interaction of process parameters on residual stress distribution.

**Keywords** finite element method · numerical model · point cloud · residual stress · smooth particle hydrodynamics · thermal barrier coating · thermal spray coatings

## Introduction

Thermal spray coating (TSC) is a type of advanced coatings that are thermally deposited on a substrate surface by heating the coating material to a molten state (Ref 1). They are used extensively for various applications that require improved substrate surface properties such as thermal resistance. Due to the presence of numerous defects (e.g., pores, cracks, splat interfaces, second-phase particles, etc.) and complex interaction between process parameters, nonlinear residual stress profile is developed along the width and thickness of the coatings (Ref 2). The process parameters which greatly influence residual stress field are droplets size, droplets temperature, droplets impact velocity, initial substrate temperature, the surface roughness (or undulation) of the substrate, spray angle/path, spray rate, gun speed and standoff distance. The adhesion strength, cohesive strength, thermal shock resistance, thermal fatigue life, corrosion resistance, wear properties and service life of coatings are affected by the residual stress field (Ref 3, 4).

Residual stress evolution in TSCs is highly complicated as it is strongly dependent on material types, process parameters and process history; thus, stresses are developed at both deposition and post-deposition regimes. Deposition stresses develop because of sudden solidification of splats, peening action of droplets on pre-deposited splats, high thermal gradient or geometric discontinuities developed during deposition. Post-deposition stresses

✉ Abul Fazal M. Arif  
afmarif@kfupm.edu.sa; afmarif1@gmail.com

<sup>1</sup> Mechanical Engineering Department, King Fahd University of Petroleum and Minerals, Dhahran, Saudi Arabia

<sup>2</sup> Mechanical Engineering Department, University of Toronto, Toronto, Canada

develop due to a mismatch in properties during cooling the coating to room temperature. Various factors such as substrate geometry, substrate surface roughness, substrate surface pretreatment and coating post-treatment have a significant influence on the residual stress state. The final residual stress distribution in the coating and substrate is a superposition of stresses developed at various length and time scales.

Various analytical models for estimation of residual stresses in coatings have been developed. But these models are usually inaccurate due to the adoption of several necessary assumptions during derivation (Ref 5). The analytical model by Tsui and Clyne (Ref 5) combined the quenching and post-deposition mismatch stresses. However, the model cannot capture nonlinearity of residual stress profile developed because of nonlinear deformation that occurs during the spray process. Consequently, several numerical models are commonly used to predict residual stresses and many researchers used the element birth-kill (FEM) approach (Ref 6). This approach was suitable as it integrates both deposition and post-deposition stresses during the computation. However, the stress results predicted with the approach were found to be only qualitatively comparable to previous experimental measurements. Wang et al. (Ref 7) integrated the birth–death approach with a micromechanics model in order to capture local stress fluctuation near defects. Wu et al. (Ref 8) reported a modified element birth–death model where a group of soft hypothetical elements with suitable properties was added at appropriate locations in order to reduce mesh distortion and improve the accuracy. But, even this approach failed to capture the local stress fluctuation. Elhoriny et al. (Ref 9) and Berthelsen et al. (Ref 10) recently proposed that the coating elements should be activated block-by-block (instead of layer-by-layer) in order to capture the local stress fluctuation due to the complex interaction between process parameters. But, even this model failed to capture local stress fluctuation occurring near the defect. For this reason, image-based finite element schemes were used to model residual stresses based on real microstructure images captured through optical micrographs, SEM or  $\mu$ -CT scan (Ref 11, 12, 13). Although this approach captured defects and the variation in residual stress field, the magnitudes of the residual stresses are expected to be inaccurate as deposition stresses developed during splats solidification were not considered during the analysis. Consequently, unrealistically high-stress values were obtained. Therefore, there is need to integrate residual stress computation with thermal spray process modeling to numerically capture important phenomena such as stress relaxation mechanisms, the presence of microstructural heterogeneities, deposition stresses and interaction of process parameters during the computation.

The numerical modeling of thermal spray process has been very challenging due to various difficulties encountered during computation such as excessive mesh distortion, computational intensity and multiple droplets interaction. Due to convergence difficulties associated with severe mesh distortion, Lagrangian grid-based schemes have been rarely used to model multiple droplets deposition occurring during the thermal spray process. Similarly, Eulerian schemes (such as phase field, level-set and the volume of fluid) are not suitable due to the coalescence of domain interfaces and high computational costs. Therefore, the thermal spray process deposition should be modeled using an alternative scheme that is not only robust but also computationally inexpensive. Recently, meshless Lagrangian methods (such as smooth particle hydrodynamics—SPH and discrete gradient method—DGM) are commonly used to model large deformation problems on point cloud (PC) with less numerical difficulties and lower computational costs. Due to its level of advancement, SPH is more popular, robust and computationally inexpensive than DGM, especially when applied to fluid problems. Consequently, Zhang (Ref 14, 15) and Farrokhpahan et al. (Ref 16) used SPH to model droplet impact and solidification during the thermal spray process. However, they could not couple the deposition process with residual stress evolution due to tensile instability arising during the computations. Despite previous attempt (Ref 17), complete elimination of the problem of tensile instability in SPH domains (subjected to high tensile stresses) is currently not achievable. Thus, SPH cannot be used to effectively model the evolution of residual stresses in TSCs. In view of this, SPH should only be used to model the dynamics of splats formation during coating deposition.

In the present study, a hybrid computational approach is used to model splat formation, the interaction between splats and evolution of residual stresses in thermal spray coating made of yttria-stabilized zirconia (YSZ) applied to steel alloy. The hybrid approach combines process modeling on point cloud (PC) with a thermo-mechanical analysis of finite elements (FEs). Smooth particle hydrodynamics (SPH) is used to model multiple droplets impact, spread and interactions on the PC, while finite element method (FEM) is used to model the heat transfer and structural deformation occurring during the spray process. This is the first contribution where coupling between SPH and FEM is used to evaluate residual stress formation in coatings. Unlike in previous models, latent heat release during splat solidification is considered during the heat transfer analysis in addition to conductive and convective heat transfer. Furthermore, both thermal-deposition (or quenching) and thermal-mismatch (post-deposition) stresses are combined to compute the final residual field. The predicted residual stress profile is validated by

comparison with experimental results obtained from the hole drilling method and previous numerical results available in the literature.

## Mathematical Model

The governing equations required are the flow (Navier–Stokes’) equation for multiple droplets deposition (Eq 1 and 2), energy equation for heat transfer (Eq 4) and local-force (stress-equilibrium) equation (Eq 7) for thermal stresses. Due to differences in length scales, the equations were developed such that only sequential coupling terms are considered. Thus, the process model involves only solving the flow equation, while for the thermo-mechanical model, the stress terms are not considered in the energy equation.

The Navier–Stokes’ equations for laminar, viscous and semi-incompressible fluid flow are given as:

$$\frac{\partial \rho}{\partial t} + (\rho v_i)_{,i} = 0 \quad (\text{Eq 1})$$

$$\rho \frac{\partial v_i}{\partial t} + \rho v_j v_{i,j} = \rho b_i + (-p \delta_{ij} + \tau_{ij})_{,j} \quad (\text{Eq 2})$$

where  $\rho$  is the density of droplet,  $v_i$  is the fluid velocity field,  $b_i$  is body force per unit volume,  $p$  is pressure,  $\tau_{ij}$  is viscous shear stress, and  $t$  is time.

Due to semi-incompressibility, a small change in pressure density is defined according to the linear form of the popular Mie–Grüneisen equations of state as:

$$p = \frac{\rho_0 c_0 \eta}{(1 - s\eta)^2} \left( 1 - \frac{\Gamma_0 \eta}{2} \right) + \Gamma_0 \rho_0 E_m \quad (\text{Eq 3})$$

where  $\rho_0$  is the reference (or initial) density,  $E_m$  is specific internal energy, and  $\Gamma_0$ ,  $c_0$  and  $\eta$  are all material constants obtained by fitting to experimental data.

Based on Fourier’s law, the final form of the energy equation written in enthalpy form is given by:

$$\rho \frac{\partial h}{\partial t} = -k T_{,ii} \quad (\text{Eq 4})$$

where  $h$  is enthalpy,  $k$  is thermal conductivity, and  $T$  is temperature.

The change in enthalpy is related to temperature and specific heat capacity as:

$$dh(T) = C_p(T) dT \quad (\text{Eq 5})$$

The specific heat capacity ( $C_p$ ) is given by:

$$C_p(T) = C_{ps}(T) + \frac{L_f}{T_m} \cdot \varphi + C_{pl} \quad (\text{Eq 6})$$

where  $C_{ps}$  is specific heat capacity of the solid material,  $C_{pl}$  is specific heat capacity of the liquid material,  $L_f$  is latent

heat of fusion, and  $\varphi$  is a Dirac-delta function with nonzero values outside the mushy zone.

Based on Hooke’s law, the final form of local-force balance equation is given by:

$$\rho \frac{\partial^2 u_i}{\partial t^2} = \sigma_{ij,j} + \rho b_i \quad (\text{Eq 7})$$

where  $u_i$  is displacement field,  $\sigma_{ij}$  is stress tensor,  $\rho$  is density,  $b_i$  is body force per unit mass, and  $\frac{\partial^2 u_i}{\partial t^2}$  is directional acceleration.

The stress tensor is related to the strain tensor ( $\varepsilon$ ) through the Hooke’s law as represented in Eq 8:

$$\sigma_{ij} = C_{ijkl} : (\varepsilon_{ij} - \varepsilon_{ij}^{th} - \varepsilon_{ij}^{pl}) \quad (\text{Eq 8})$$

$$\varepsilon_{ij} = \varepsilon_{ij}^{el} + \varepsilon_{ij}^{th} + \varepsilon_{ij}^{pl} \quad (\text{Eq 9})$$

where  $\varepsilon_{ij}^{el}$  is elastic strain tensor,  $\varepsilon_{ij}^{th}$  is thermal strain tensor, and  $\varepsilon_{ij}^{pl}$  is plastic strain tensor.

Due to the large temperature difference between the coating and substrate materials, large deformation usually occurs coating deposition. Thus, based on large-strain formulation, the total strain is related to the displacement fields by:

$$\varepsilon_{ij} = \frac{1}{2} (u_{i,j} + u_{j,i} + u_{k,i} \cdot u_{k,j}) \quad (\text{Eq 10})$$

The thermal strain is developed due to the mismatch in the coefficient of thermal expansion between the coating and substrate materials. It is usually expressed as:

$$\varepsilon_{ij}^{th} = \int_{T_{ref}}^T \alpha(T) \cdot dT \quad (\text{Eq 11})$$

Using the von Mises criterion, the flow rule for the plastic deformation can be represented by:

$$d\varepsilon_{ij}^p = d\lambda \frac{\partial Q}{\partial \sigma_{ij}} = \frac{3}{2} d\lambda \frac{S_{ij}}{\sigma_{eq}} \quad (\text{Eq 12})$$

where  $d\varepsilon_{ij}^p$  is an increment of the plastic strain tensor,  $Q$  is yield function,  $S_{ij}$  is deviatoric stress tensor,  $\sigma_{eq}$  is equivalent stress and  $d\lambda$  is a plastic multiplier which is a scalar function of plastic strain.

The equivalent stress based on von Mises yield criteria is usually expressed as a function of deviatoric stress tensor as:

$$\sigma_{eq} = \sqrt{\frac{3}{2} S_{ij} : S_{ij}} \quad (\text{Eq 13})$$

Due to its brittleness, the ceramic coating layer does not undergo strain hardening or plastic deformation. Thus, it is only required to restrain tensile stresses developed in the presumably microcracked ceramic layer to low values

using perfectly plastic material model [as used in recent works (Ref 8)]. For the substrate material (i.e., a metal), the yield surface is assumed to evolve based on the Johnson–Cook model as shown in Eq 14.

$$Q = \sigma_{eq} - \sigma_{yp} \leq 0 \quad (\text{Eq 14})$$

with initial yield surface, as:

$$\sigma_{yp} = \left[ A + B(\bar{\epsilon}^{pl})^n \right] \left[ 1 + C \ln \left( \frac{d\bar{\epsilon}^{pl}}{d\bar{\epsilon}_0^{pl}} \right) \right] (1 - \hat{\theta}^m) \quad (\text{Eq 15})$$

where  $\bar{\epsilon}^{pl}$  is equivalent plastic strain variable,  $\hat{\theta}$  is non-dimensional temperature,  $A$ ,  $B$ ,  $m$ ,  $n$  and  $\bar{\epsilon}_0^{pl}$  are all material constants to be obtained by fitting with experimental data.

**Initial Conditions** The initial parameters for the process model are the diameter, impact velocity and temperature of sprayed droplets. The process model is developed such that deposition is carried out in a layer-by-layer manner having a fixed number of droplets (i.e., 9 droplets in this case) released at each step. For more realistic analysis, the process parameters are defined to have random values which fall within the range of statistical data given in the previous experiment by Xue et al. (Ref 18) (as demonstrated in Fig. 1). Thus, the droplets have random initial diameters, impact velocities and temperatures ranging from 29 to 32  $\mu\text{m}$ , 100–110 m/s and 2535–2550  $^{\circ}\text{C}$ , respectively. The substrate dimensions are selected based on the volume required for proper dissipation of the heat during the process. Any form of heat transfer during droplet flight is neglected. According to the usual practice, the substrate material is pre-heated to reduce deposition stresses and improve coating adhesive strength; thus, the substrate layer is at an initial temperature of 700  $^{\circ}\text{C}$ .

**Boundary Conditions** For the process model, the wall boundary condition is applied at the interface between the droplets and substrate or pre-deposited layer surfaces as:

$$v_{i-\text{fluid}} = v_{i-\text{solid}} \text{ at fluid - structure interface} \quad (\text{Eq 16})$$

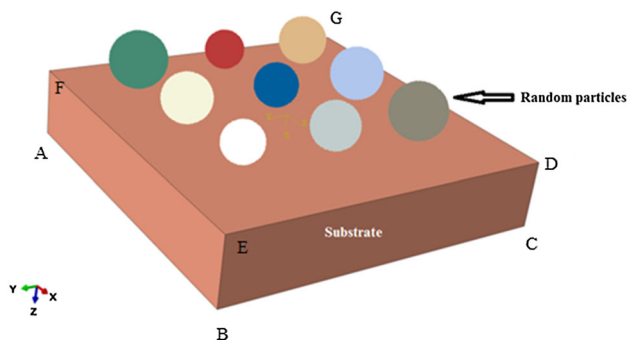


**Fig. 1** Release/impact of sprayed droplets on substrate in layer-wise fashion (vertex  $O$  shares the same edge with  $G$ )

where  $v_{i-\text{fluid}}$  is velocity of fluid and  $v_{i-\text{solid}}$  is velocity of solid.

For the thermo-mechanical model, convective boundary conditions are applied on all boundaries of the substrate and exposed surfaces of pre-deposited splats such that temperature is fully dissipated in all directions. Symmetrical boundary conditions are applied at boundaries OAFG and OCDG. As done in the works of Klusemann et al. (Ref 11), Nayeypashae et al. (Ref 19) and Gupta (Ref 20), the boundaries ABEF and BCDE are constrained to deform uniformly in the  $y$ - and  $x$ -direction, respectively. To avoid any rigid body motion by substrate geometry, one node at the origin (i.e., vertex  $O$ ) is constrained from moving in all directions. For simplicity, perfect bonding is assumed between splat–substrate and splat–splat interfaces as used in previous research works (Ref 8, 9).

$$q_i = -kT_{i,i} = h_{cv}(T - T_a) \text{ at all exposed surfaces} \quad (\text{Eq 17})$$

where  $h_{cv}$  is convective heat transfer coefficient.

$$n_i u_i = 0 \text{ at faces OAFG and OCDG} \quad (\text{Eq 18})$$

where  $n_i$  is unit normal vector

$$u_i = 0 \text{ at one point } O \quad (\text{Eq 19})$$

**Material Models** Due to large temperature changes associated with the process, the stainless-steel substrate is modeled using Johnson–Cook material model which accounts for the influence of temperature and loading rate on its yield strength. The initial substrate temperature (700  $^{\circ}\text{C}$ ) is taken as the reference temperature for stress computation. As used in recent works (Ref 8), the perfectly plastic model has been used to restrict tensile deposition stresses to lower values to consider stress relaxation (through microcracking) within the ceramic coatings when under high tensile stresses. Consequently, the ceramic coating has lower yield strength in tension as compared to compression. Thermal, fluid and structural properties used in the current model are given in Table 1.

## Numerical Model

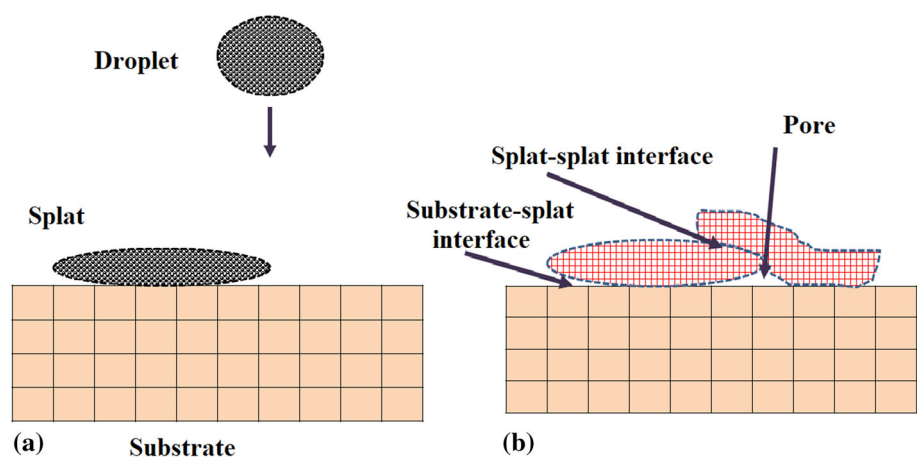
The computational approach used is hybrid in the sense that it combines two different numerical methods, SPH and FEM, to predict residual stress evolution in thermal spray coatings (TSCs) as shown in Fig. 2.

## SPH Formulation

According to SPH formulation, the flow or deformation of continuum bodies is represented using sets of particles

**Table 1** Material properties used for the simulation

Property	YSZ (Ref 14, 21–23)	301 stainless steel (Ref 14, 21, 24)
<i>Fluid properties</i>		
Density, $\rho$ (kg/m <sup>3</sup> )	5890	7900
Viscosity, $\mu$ (kg/ms)	0.008	...
Speed of sound, $c_0$ (m/s)	3000	...
Dimensionless parameter, $s$	2.39	...
Dimensionless parameter, $\Gamma_0$	0	...
<i>Phase change properties</i>		
Latent heat, $L$ (J/kg)	$7.07 \times 10^5$	...
Specific heat capacity, $c_p$ (J/kg K)	713 @ 2535 °C 580 @ 2522 °C	477
Thermal conductivity $k$ (W/m K)	2.32 @ 2535 °C 2.0 @ 2522 °C	14.9
Coefficient of thermal expansion (CTE), $\alpha$ (/°C)	$9.68 \times 10^{-6}$ @ 20 °C $10.34 \times 10^{-6}$ @ 1000 °C $11/22 \times 10^{-6}$ @ 2527 °C	$16.6 \times 10^{-6}$ @ 100 °C $17.6 \times 10^{-6}$ @ 300 °C $18.6 \times 10^{-6}$ @ 500 °C $19.5 \times 10^{-6}$ @ 700 °C
Heat transfer coefficient of air, $h_{cv}$ (W/m <sup>2</sup> K)	20	20
<i>Structural properties</i>		
Elastic modulus/Poisson's ratio, $E$ (GPa)/ $\nu$	63.40/0.21 @ 20 °C 28.33/0.21 @ 2000 °C 26.67/0.21 @ 2522 °C $3 \times 10^{-3}$ /0.4 @ 2532 °C $3 \times 10^{-3}$ /0.4 @ 3000 °C	200/0.3 @ 700 °C 0.2/0.4 @ 1400 °C
Yield strength, $\sigma_y$ (MPa)	30 (tensile) 300 (compressive)	Based on Johnson–cook the following parameters: $A = 310$ , $B = 1000$ , $C = 0.07$ , $n = 0.65$ , $\dot{\epsilon} = 1/s$ and $m = 1$

**Fig. 2** Hybrid computational approach: (a) droplets impact, spread and interaction using SPH, (b) splats solidification and residual stress evolution using FEM

which have unique material properties (such as density, viscosity, pressure). The solution across the domain is obtained using the kernel (or smoothing) functions.

SPH formulation for the Lagrangian form of conservation of mass and momentum equation can be expressed as (Ref 25):



$$\frac{D\rho_i}{Dt} = \sum_{j=1}^n m_j \bar{v}_{ij} \cdot \nabla_i W_{ij} \quad (\text{Eq 20})$$

$$\frac{D\bar{v}_i}{Dt} = D - \sum_{j=1}^n m_j \left( \frac{p_i}{\rho_i^2} + \frac{p_j}{\rho_j^2} \right) \nabla_i W_{ij} + \sum_{j=1}^n m_j \left( \frac{\tau_i}{\rho_i^2} + \frac{\tau_j}{\rho_j^2} \right) \cdot \nabla_i W_{ij} + \bar{b} \quad (\text{Eq 21})$$

where  $\bar{v}_{ij}$  is the velocity of particle- $i$  relative to that of particle- $j$ ,  $W_{ij}$  is kernel (smoothing) function between particle- $i$  and particle- $j$ ,  $\rho$  is density,  $p$  is pressure,  $\tau$  is viscous stress tensor, and  $\bar{b}$  is body force. The cubic spline kernel function  $W_{ij}$ , developed by Monaghan (Ref 26), is adopted for analysis in the current work.

Using SPH particle approximation, the viscous stress tensor is usually represented as:

$$\tau_i = - \sum_{j=1}^n \frac{m_j}{\rho_j} \mu_i \bar{v}_{ij} \nabla_i W_{ij} - \sum_{j=1}^n \frac{m_j}{\rho_j} \mu_i (\nabla_i W_{ij}) \bar{v}_{ij} + \left( \frac{2}{3} \sum_{j=1}^n \frac{m_j}{\rho_j} \mu_i \bar{v}_{ij} \cdot \nabla_i W_{ij} \right) I \quad (\text{Eq 22})$$

The surface tension term is not included in the numerical model to reduce computational costs. Rather, the deposition model is calibrated to account for the effect of surface tension on splats size and spreading time using semiempirical equation (Ref 27).

### Reconstruction of Splat Geometry from PC

In this section, several algorithms used for the conversion of point cloud (PC), obtained from SPH domain to high-quality finite element (FE) mesh, are discussed.

1. *Poisson-Disk Sampling (PS)* PS algorithm [developed by Corsini et al. (Ref 28)] is used to increase the density of point cloud such that the point sets are sufficient for effective mesh generation. The algorithm does not add points outside the domain of interest.
2. *3D Alpha-Shape* 3D alpha-shape algorithm [first developed by Edelsbrunner and Mücke (Ref 29) and recently improved by Kamberov et al. (Ref 30)] is used to reconstruct the surface topology of objects from point cloud data. The algorithm requires the user to provide an optimum  $\alpha$ -value depending on the complexity of the shape. When the  $\alpha$ -value is too small, unwanted cavities emerge on the surface, while larger  $\alpha$ -value results in a rough surface.
3. *Poisson Surface Reconstruction (PSR)* PSR algorithm [developed by Kazhdan and Hoppe (Ref 31, 32)] is used for generation of an implicitly represented surface from the dense point cloud. Based on theory, Poisson's equation is used to compute an implicit scalar function

that fits the original surface with minimum error (or deviation). The algorithm is generally faster and more robust than other implicit surface reconstruction methods (such as RBF, least squares, distance function, the multi-level partition of unity implicit). The only drawback is that it needs consistent normal orientation for effective generation of stereolithographic (STL) mesh.

4. *Quadratic Edge Decimation (QED)* QED algorithm [developed by (Ref 33)] reduces the number of simplicial complexes in a given polytype iteratively with little compromise on shape, size and computational costs. The algorithm is used to reduce the density of the STL mesh to the required number of elements. Thus, two vertices along an edge of element degenerate into a single vertex which reconnects with other simplified vertices to form a new edge. The new position of the vertices and length of new edges for the polytype are determined by optimizing the quadratic error metric iteratively.
5. *Least Square Subdivision Surface (LS3)* LS3 algorithm is used re-smooth the surface of an object in such a way that a coherent STL mesh results. The algorithm repositions vertices of the mesh such that the square of distances from the points to its nearest neighbors is least. Details about this algorithm and implementation should be checked elsewhere (Ref 34).
6. *STL-FE Mesh Conversion* This is the last stage of the geometric reconstruction step where the generated STL (surface) mesh is converted into a solid 3D FE mesh. In most of recent commercial CAD/FE packages (such as ABAQUS, COMSOL and ANSYS), there exist several options for this task. For instance, ABAQUS packages have an option of importing STL mesh and directly converting the 2D trigonal elements into 3D tetrahedral elements using the in-built algorithm. Details for this can be found elsewhere (Ref 35).

### Finite Element Formulation

Using the converted FE mesh of splats, a thermo-mechanical analysis is to be conducted for the prediction of the evolution of temperature and stresses. Using Galerkin's finite element approximation and backward Euler time stepping scheme, the variational form of the energy equation can be given in discrete form as:

$$\int_V [N]^T \cdot \rho(T) \cdot \frac{d}{dt} \{H\} dV + \int_V [B]^T \cdot k(T) \cdot [B] dV - \int_{A_h} [N]^T \cdot h_{cv}(T) \cdot (T - T_{air}) dA = 0 \quad (\text{Eq 23})$$

where  $\rho(T)$  is density,  $\{H\}$  is nodal enthalpy matrix,  $k(T)$  is thermal conductivity,  $[N]$  is element interpolation (or shape) function matrix,  $[B]$  is shape function derivative matrix,  $h_{cv}(T)$  is convection heat transfer coefficient on external boundaries, and  $T_{air}$  is ambient temperature.

Using Newton's iteration to linearize Eq 23, we obtain the following discretized form of the equation as:

$$[K_{th}]\{\Delta T_{i+1}^{t+\Delta t}\} = \{R_t\} \quad (\text{Eq 24})$$

where

$$\begin{aligned} [K_{th}] &= \int_V [N]^T \cdot \rho(T) \cdot \left( \frac{dH}{dT} \right)_i^{t+\Delta t} [N] dV \\ &+ \int_V [B]^T \cdot k_i^{t+\Delta t}(T) \cdot [B] dV - \int_{A_h} [N]^T \cdot h_{cv}^t(T) \cdot [N] dA, \\ \{R_t\} &= \int_{A_h} [N]^T \cdot h_{cv}^t(T) \cdot (T_i^{t+\Delta t} - T_{air}) dA \\ &- \frac{1}{\Delta t} \int_V [N]^T \cdot \rho(T) \cdot (H_i^{t+\Delta t} - H^t) dV \\ &- \int_V [B]^T \cdot k^t(T) \cdot [B] dV \end{aligned}$$

and  $\Delta t$  is the time step.

Using Eq 24, the nodal temperature at each time step is found by solving the resulting algebraic form of equations. The latent heat release during the solidification process is accounted for at each time step in the term,  $\left( \frac{dH}{dT} \right)_i^{t+\Delta t}$ , representing the effective heat capacity of the material.

While the variational form of the stress-equilibrium equation (given in Eq 26) is given as:

$$\begin{aligned} &\int_V \rho(T) \cdot [N]^T \cdot \frac{d^2}{dt^2} \{U\} \cdot [N] dV \\ &= - \int_V [B]^T \cdot [\sigma] \cdot dV + \int_S [N]^T \cdot \{t\} dS \\ &+ \int_V \rho(T) \cdot [N]^T \cdot \{g\} dV \end{aligned} \quad (\text{Eq 25})$$

where  $\{U\}$  is nodal displacement vector,  $[\sigma]$  is internal stress tensor,  $\{t\}$  is boundary traction vector, and  $\{g\}$  is body force vector.

From Eq 25, it can be seen that the inertia of the system can be generally expressed as the difference between external forces ( $P_{ext}$ ) acting on the body and internal forces developed due to stress field ( $P_{in}$ ) leading to dynamic equilibrium as expressed in Eq 27,

$$[M] \cdot \frac{d^2}{dt^2} \{U\} = \{P_{ext}\} - \{P_{in}\} \quad (\text{Eq 26})$$

where  $[M]$  is the mass matrix.

For an implicit-static procedure, the stiffness matrix directly relates to the displacement field based on Newton–Raphson iteration scheme as:

$$[K]_i^{t+\Delta t} \cdot \{\Delta U\}_i^{t+\Delta t} = \{P_{ext}\}_{i+1}^{t+\Delta t} - \{P_{in}\}_i^{t+\Delta t} \quad (\text{Eq 27})$$

where  $[K] = \int [B]^T [J] [B] dV$  is the stiffness matrix and  $[J] = \frac{\partial \Delta \sigma}{\partial \Delta \epsilon}$  is the Jacobian matrix.

At each time step, the temperature distribution obtained using Eq 24 is used to compute thermal strains and corresponding internal stresses which are used to predict the displacement or deformation of the bodies.

## Numerical Implementation

Thermal spray process can be divided into sub-regimes, i.e., multiple droplets impact and spreading (occurs within 0–2  $\mu$ s), solidification of splat layers (occurs within 20–500  $\mu$ s) and post-deposition cooling to room temperature (occurs within 1–50 s). As the time scale of these regimes differs considerably, a sequentially coupled approach is adopted during the implementation of the hybrid model. Thus, the flow (Navier–Stokes') equations are solved solely for prediction of splat formation process during the first regime. Then, the reconstructed FE mesh of splat structures is used to solve for quenching stresses developed during splat solidification (i.e., second regime). Lastly, the results of the second regime are read as an initial condition for computation of mismatch stresses developed when the coated structure is finally cooled to room temperature. This coupling greatly improves the computational efficiency of the model without much compromise on results quality.

The numerical implementation was carried out in standard finite element packages (ABAQUS and MeshLab) and self-developed codes. The required initial and boundary conditions are first defined. Then, the velocity field and peening stress developed after droplets impact are solved using PC3D continuum particle elements based on SPH model (implemented in ABAQUS/Explicit). For consistency, the SPH model is calibrated such that droplets spreading stops after reaching a spreading factor that is equivalent to that of the previous semiempirical model (Ref 27). The geometry of the deposited splats (i.e., shape and size) is then extracted (in form of PC) using python codes before PC-to-FE conversion which has been fully implemented in the open-source package, MeshLab, using MLX scripts. Firstly, point cloud file which contains the number and coordinate of about 3000 points (from SPH results) is read and imported into Meshlab server. Then, the surface topology of deposited splat structures is roughly

reconstructed using 3D alpha shape with an optimum alpha value of 5% of the bounding box diagonal length (i.e., about 0.0102353 mm). The population of original PC is populated to around 2 million points using the PS algorithm. Using the 2 million points, a smoother surface topology is generated for the second time using a 3D alpha shape (with a lower alpha value of 2%). The smoothened surface is used to generate denser PC having up to 8 million points using the PS algorithm. Then, the denser PC is used to generate high-quality implicit surface (or STL mesh) using PSR algorithm (with octree depth of 7 and solver divide of 8). With insufficient PC density, the implicit surface generated by PSR algorithm may contain few holes or distorted structures. In that case, the hole sites need to be deleted and repaired using the “close hole” algorithm available in Meshlab. Before the final conversion of STL to 3D FE mesh, QED algorithm is used to reduce STL mesh density to the required level of refinement, while LS3 algorithm is used to re-position surface and improve elements aspect ratio. Upon import into ABAQUS/CAE, the STL mesh is transformed into 3D (solid) FE mesh using algorithms embedded in the software (i.e., in edit-mesh tool options). The average time required for the conversion is about 45 min per splat using 32 cores/64 GB RAM/2 GHz Dell workstation. The current process of converting the PC into FE mesh works well for all type of splats regardless of how intricate their geometry might be as shown in later sections. A typical demonstration for the conversion is demonstrated in Fig. 3. The 3D FE mesh is used for

thermo-mechanical analysis of the coating process during the second and third regimes. The heat transfer and implicit-static (post-deposition stress) model are implemented in ABAQUS/Standard using implicit time stepping scheme, while the explicit-dynamic (deposition stress) model is implemented in ABAQUS/Explicit using a conditionally stable explicit time stepping scheme. The final residual stress field is predicted by integrating the deposition stresses with that of post-deposition cooldown mismatch stresses obtained using thermostatic-structural analyses.

## Experimental Procedure

For the purpose of validation of numerical results, residual stress measurement was conducted based on hole drilling experiment (as shown in Fig. 4). A stainless-steel (SS301) substrate was first to cut into dimensions of 12 mm × 2.5 mm × 1.5 mm and grit-blasted with an alumina grit having an average diameter of 0.16 mm. Then, a thin layer of NiCrAl bond coat [of type Metco 443NS (Ref 36)] was to improve the adhesion of YSZ top coat. The YSZ top coat was deposited with conventional DC plasma torch using spherical powder of type Oerlikon Metco 204NS-G (Ref 37). The coating layer was deposited in 6 passes up to coating thickness of about 150 μm (as shown in Fig. 4c). Before the start of hole drilling experiment, the surface of the coating sample was prepared according to the

**Fig. 3** PC-to-FE mesh conversion for splats of intricate shapes

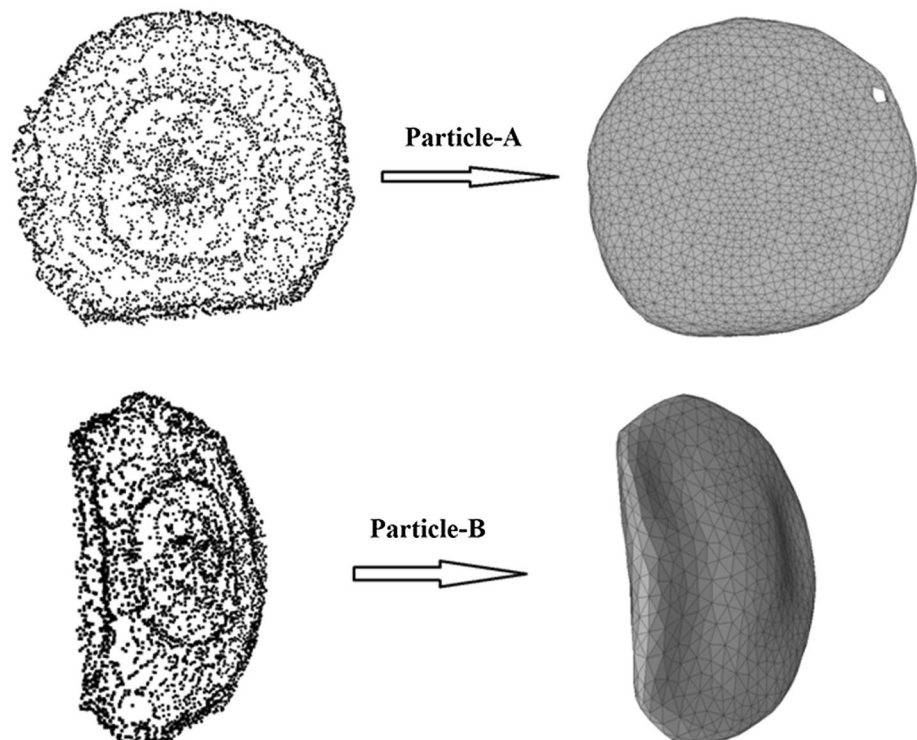
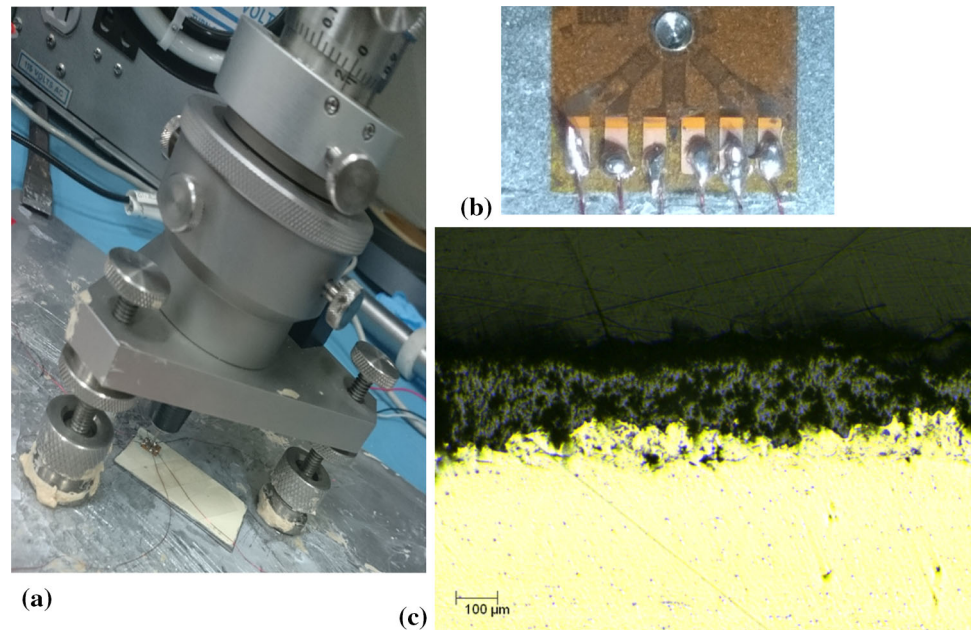




**Fig. 4** (a) Drilling of YSZ sample using HD setup, (b) bonded and soldered 062UM-type strain gauge, (c) cross section view of coating sample (optical micrograph)



procedure given in bulletin B-129-8 (Ref 38) of the manual by Vishay Micro-measurement Inc. The top surface of the sample was first cleaned with a degreaser, M-prep conditioner-A and M-prep neutralizer 5-A. This helps in establishing a strong bond between the strain gage and surface of the sample. Then, CEA-XX-062UM-120-type strain gage (having mean diameter of 5.13 mm) was bonded to the surface using M-bond 200 adhesive as explained in bulletin B-127-4 (Ref 39). The terminals of the strain gage were connected to the P3 strain gage indicator using lead wires and three-wire quarter bridge circuit. The HD device was installed and aligned properly above the strain gage according to the RS-200 Milling Guide (Ref 40). Diamond-coated tungsten carbide cutter with a diameter of 1.4 mm was used to drill through the strain gauge using an air turbine. It is essential to limit the drilling rotational speed and feed rate to minimize the influence of cutting forces and sample overheating on strain readings. After the establishment of the zero depth, the hole drilling was started, and strain readings were taken in increments of 20 μm and feed rate of 5 μm/min until attaining a total depth of 600 μm. Before taking readings, it was necessary to wait for at least 10 min for the ceramic sample to cool down and strain readings to stabilize. The multilayered nature of coated samples necessitates the use of finite element analysis to compute the calibration coefficients required for the estimation of residual stress profile. This task was carried in ABAQUS/Standard environment, and the popular differential method was used for residual stress calculation as previously done by Gadow et al. (Ref 41) and Buchmann et al. (Ref 42, 43).

## Results and Discussion

In the present study, a hybrid computational approach for the numerical modeling of residual stress evolution in thermal spray coatings (TSCs) is tested on thermal barrier coating (TBC) system made of yttria-stabilized zirconia (YSZ) deposited on steel alloy. The predicted residual stress profile has been validated by comparing with results obtained from the analytical model by Tsui and Clyne (Ref 5) and hole drilling experiments. Using this new computational approach, the effect of influential process parameters (such as droplet size, impact velocity, temperature, impact angle, spray path and substrate surface roughness) on the residual stress profile can be properly investigated.

### Multilayer Deposition with SPH

For a complete assessment of efficiency and accuracy of the proposed approach, several tests are carried out based on single droplet deposition on a flat substrate. Figure 5 shows that the results predicted using the current SPH model is reasonably comparable to those of previous experiments (Ref 44), and numerical results obtained using Coupled–Eulerian–Lagrangian (CEL) approach (Ref 21). The spreading time of the droplet which has an initial impact velocity of 190 m/s is comparable to that of the CEL model, i.e., 0.39 μs. The results also show that higher initial impact velocities result in higher spread factor with slight deviation observed between the SPH results and those of the CEL.

Using statistically defined initial conditions, multiple droplets deposition is modeled on PC using SPH. The

computation is carried out layer-wise up to the fifth layer of deposition. For brevity, only results of the second and fourth layer will be presented here. Figure 6(a) and (b) shows the variation of the velocity component in the  $z$ -direction during droplets deposition for the second and fourth layers (each consisting of nine droplets). Due to the low impact energy associated with APS process, peening stresses are not considered in the present study. The average spreading time for the droplets is found to be about  $1\ \mu\text{s}$  which is comparable to times reported in previous studies (Ref 14, 45). The average spread factor, diameter and thickness of the simulated splats are found to be 3.47,

79.2 and  $4.2\ \mu\text{m}$ , respectively. The size and shape of deposited splats are found to be strongly influenced by their interaction with nearby droplets, thereby resulting in complex splat geometries. Consequently, the simulated coating microstructure developed in current work has a variety of discontinuities or imperfections (such as pores, cracks and other complex geometrical features) typically encountered in thermal spray coatings.

## Thermo-Mechanical Analysis

### Simulated Coating Microstructure

Upon completion of multiple droplets deposition in layers, the geometry of each splat is reconstructed using the various algorithms described in [Numerical Model](#) section. The geometry is first represented in the form of STL (or surface) mesh which contains high-quality trigonal elements. Then, the STL mesh is transformed into a 3D linear tetrahedral mesh using edit-mesh tool options of ABAQUS/CAE. Through stacking of multiple splats, we developed a numerical coating microstructure with good overlap at splats interface as shown in Fig. 7. We found that meshing splat bodies in ABAQUS results in higher computational efficiency and minimized numerical issues (arising due to poor elements) as compared to when it is done elsewhere. Also, grid-independence test was carried out to ensure that the level of mesh refinement is sufficient for numerical convergence at a moderate computational cost. The average size of elements within each layer is demonstrated in Table 2 (in the form of average edge lengths). The criteria for mesh quality are that ABAQUS

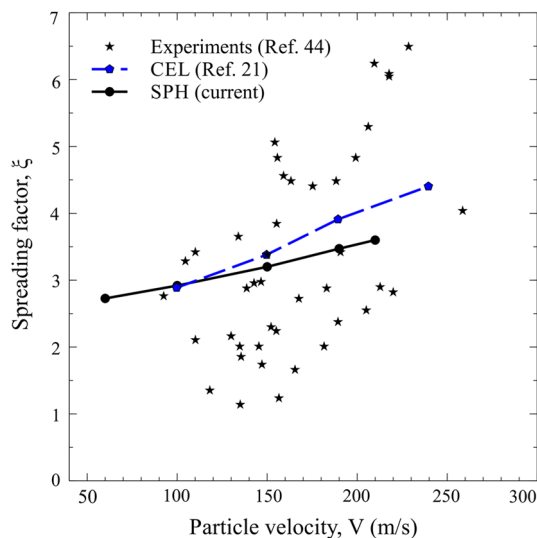


**Fig. 5** Validation of SPH model for droplet deposition

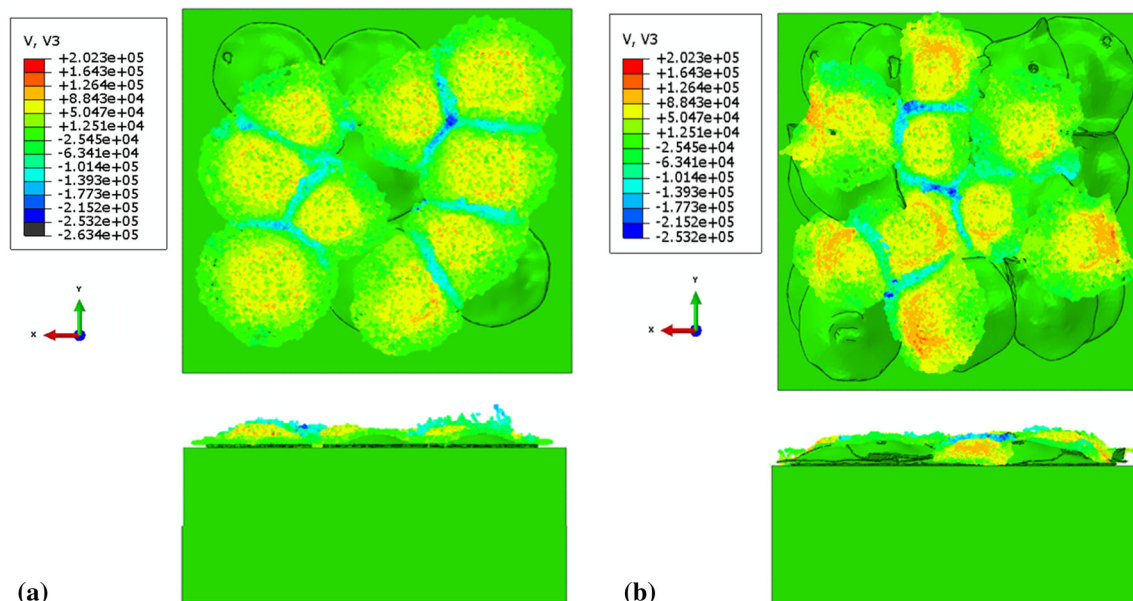


**Fig. 6** Velocity of droplets in impact direction (mm/s) during deposition of (a) second layer and (b) fourth layer

accepts any tetrahedral element that has a shape factor of at least  $3 \times 10^{-3}$ , face corner angle within 5 and 170 and aspect ratio of at most 10. Upon preliminary checks, we found that the mesh generated with current approach passed the overall criteria despite the presence of discontinuities (as demonstrated in Table 2). Even deleting the very few elements that failed some of the criteria makes no

difference in terms of results quality. The approach adopted here is more suitable and flexible as compared to the popular image-based finite element approach. Apart from having finite elements of higher quality, it is developed based on standard codes available in the literature. Thus, it does not involve tedious noise cleaning and re-processing of microstructure images. The approach also captures the process dependence and layer-wise build-up of temperature and residual stress during the spray process.

### Temperature Distribution

Figure 8(a) and (b) shows the temperature distribution developed after the deposition of the second and fourth layers, respectively. The figures show that the newly deposited splat layer (in gray) starts to solidify after its contact with the pre-solidified coating layers. The prediction of temperature distribution for the first and second layer is more computationally demanding due to the steep gradient developed near the interface. It is also found that the solidification rate of a given splat is immensely affected by its interaction with its nearest neighbors. Consequently, partial re-melting of pre-solidified splats (due to contact with new splats) is observed in certain regions. Thus, the numerical results predicted here show that temperature distribution is not only complex but highly dependent on many factors such as geometrical complexity, a number of layers deposited, solidification rate, quality of contact and other factors which should be considered for effective prediction of residual stress evolution.

As shown in Fig. 9, five points are selected for quantitative analysis of temperature and stress profiles developed along the thickness of the coating layer. Figure 10 shows

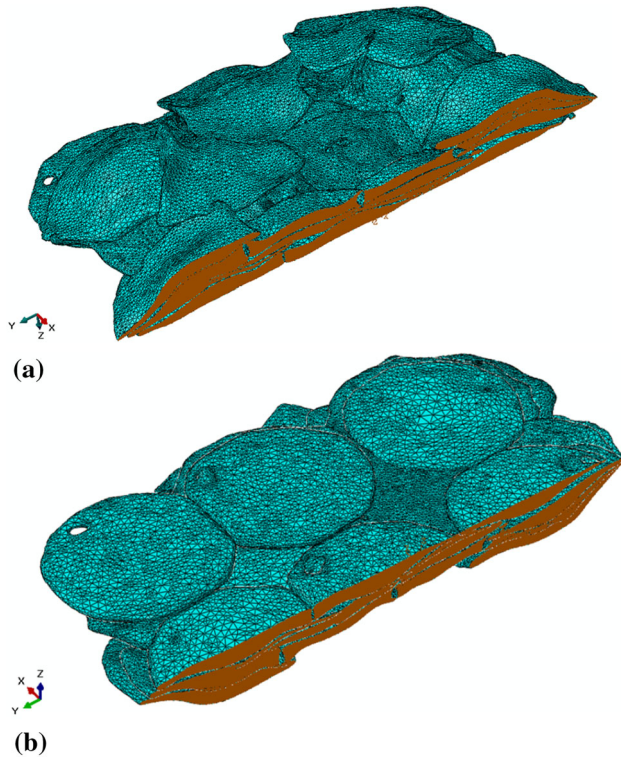


**Fig. 7** 3D tetrahedral FE mesh of splats deposited in five layers

**Table 2** Information on tetrahedral element size and quality

Layer name	First	Second	Third	Fourth	Fifth
# Splats	9	9	9	9	9
# Elements	124,591	90,499	60,418	96,119	60,432
# Nodes	31,314	19,566	15,965	20,335	16,317
Shape factor < 0.0001: average/worst/# Elem.	0.6085/2 × 10 <sup>-2</sup> /0	0.5721/1 × 10 <sup>-5</sup> /1	0.5973/4 × 10 <sup>-6</sup> /4	0.5668/1 × 10 <sup>-10</sup> /6155	0.6/1.1 × 10 <sup>-4</sup> /0
Min angle < 5: average/worst/ #Elem.	36.17/7.97/0	35.93/4.83/0	35.69/3.42/1	36.12/5.00/1	35.81/4.35/1
Max angle > 170: average/worst/#Elem.	91.56/150.90/0	91.95/168.65/0	92.39/170.21/1	91.64/163.76/0	92.03/169.27/0
Aspect ratio > 10: average/worst/# Elem.	1.75/6.14/0	1.77/8.93/0	1.80/10.23/1	1.76/8.79/0	1.78/7.43/0
Average min. edge length (μm)	1.65	1.82	2.13	1.76	2.19
Average max. edge length (μm)	2.81	3.23	3.66	3.00	3.76

#Elem. number of elements that failed the criteria



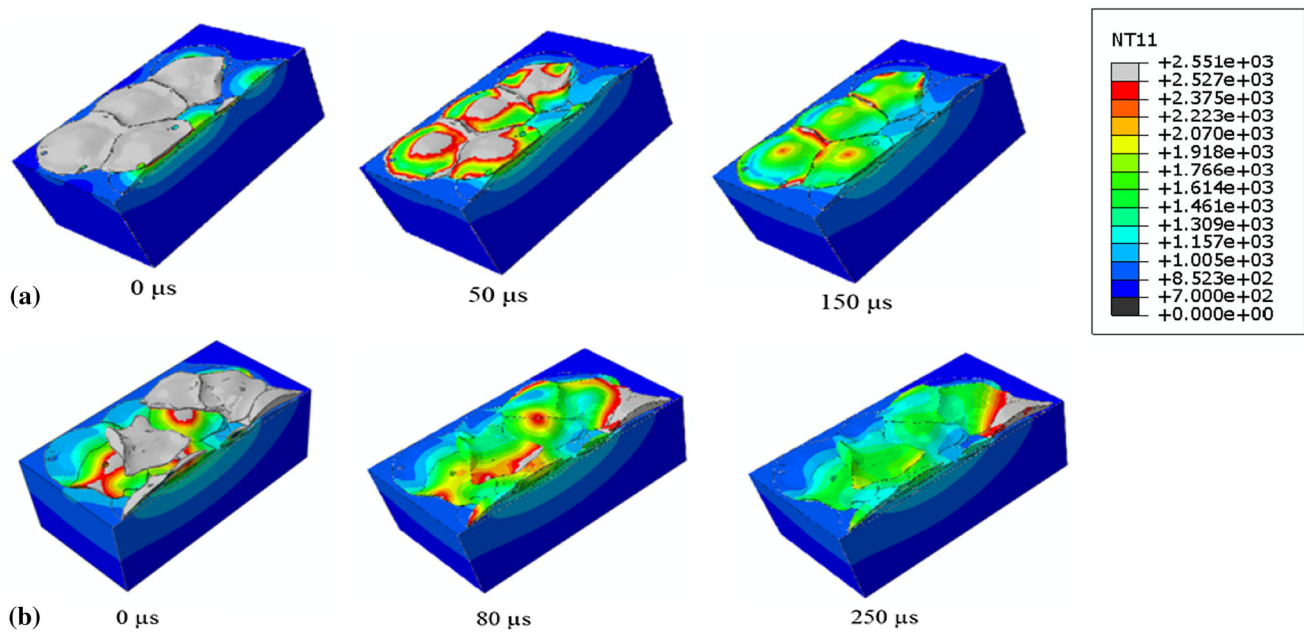


**Fig. 8** Evolution of temperature (°C) during splats solidification for: (a) second layer and (b) fourth layer

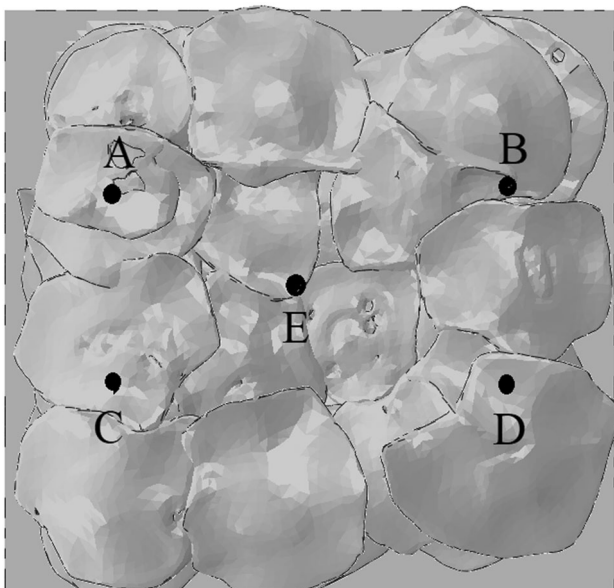


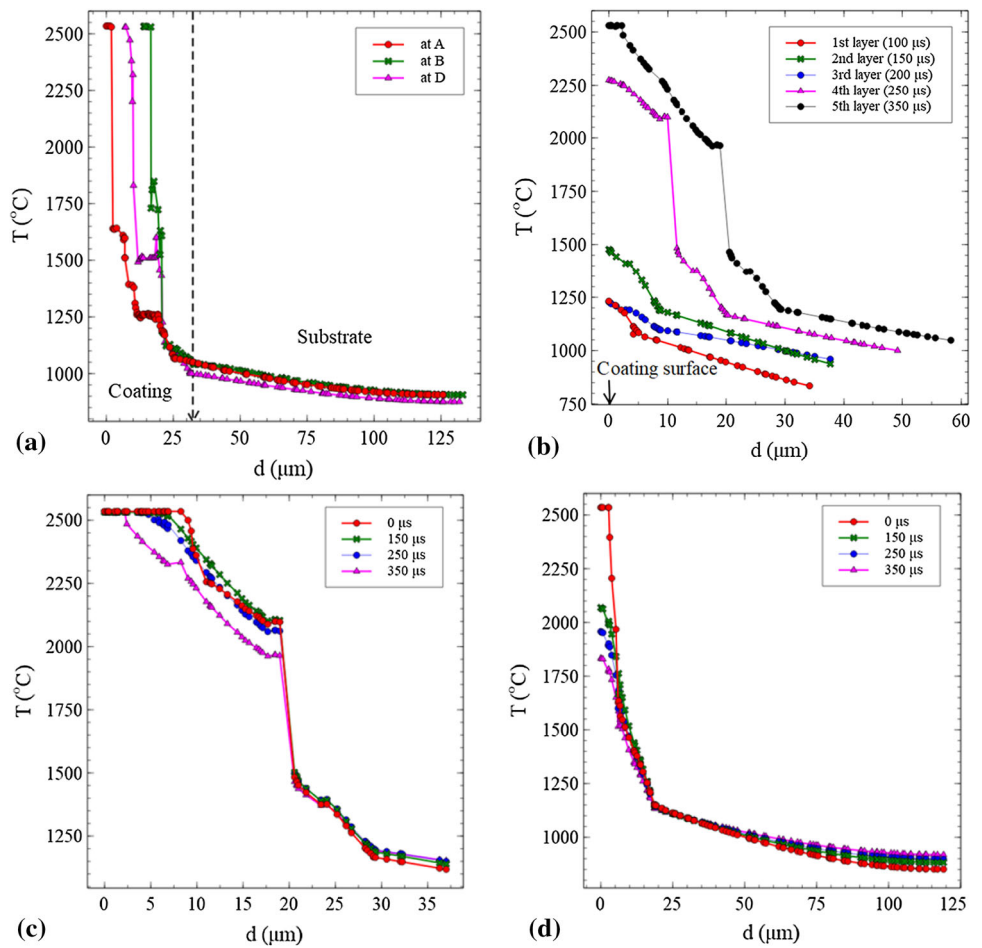
**Fig. 9** Five points selected for the analysis of results

the variation in temperature along the thickness direction after solidification of the fifth splat layer. As observed experimentally, the coating layer has a variable thickness due to undulation resulting from the interaction of multiple splat layers (shown in Fig. 10a). Thus, the simulated microstructure has a larger thickness (around 15–30  $\mu\text{m}$ ) at points A, C and D as compared to points B and E (5–10  $\mu\text{m}$ ). Figure 10(b) shows that the high-temperature

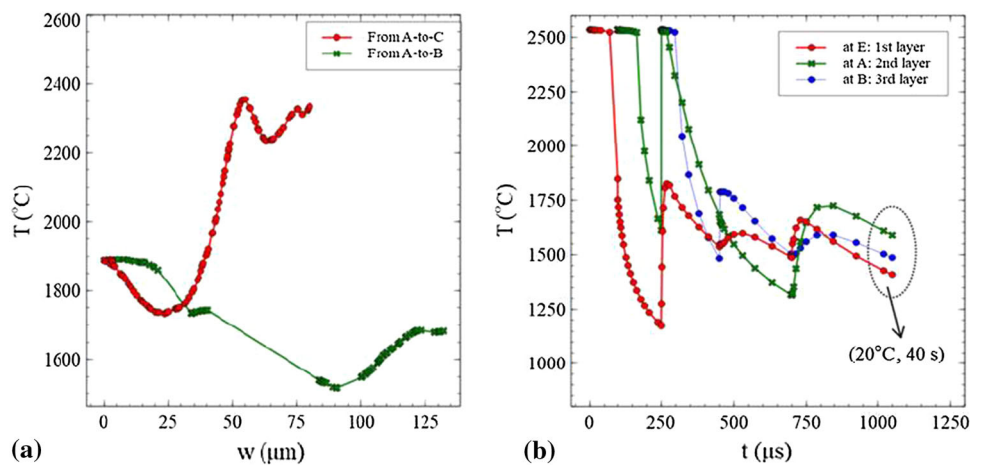
gradient developed along the thickness of the coating decreases with an increase in coating thickness, resulting in a decrease in the solidification rate with the deposition of more splat layers. Figure 10(c) and (d) shows the variation in temperature during the deposition of the fifth layer at points C and E. It can be seen that the temperature of the coating layer drops from the melting point to lower values during deposition, while that of the substrate rises. There is a sharp drop in temperature in some regions within the coating layer due to the presence of pores or cracks. Consequently, the temperature profile varies from point to point because of the influence of complex geometrical features on temperature distribution.

Figure 11(a) shows the variation in temperature along the width and length of the coating. The thermal gradient developed along those directions is far lower as compared to that along the thickness direction. Consequently, it is expected to have less stress variation along that direction. Figure 11(b) shows that the thermal histories of three different points (A, B and E) located at different layers are not only different but highly random due to the complex nature of the process. As observed from the figure, the temperature at those points overshoots to higher values after a certain time due to several cycles of reheating caused by the deposition of new splat layers. It is expected for the coating layer to develop complex residual stress field within the coating microstructure due to the strong dependence of temperature with location and process history.

**Fig. 10** (a) Temperature profile developed after solidification of 5th layer at different locations, (b) temperature profile developed after solidification of 1st–5th layer, (c) evolution of temperature during deposition of 5th layer at C and (d) evolution of temperature during deposition of 5th layer at E



**Fig. 11** (a) Temperature profile along coating width and length; (b) temporal variation of temperature from deposition to end of cooldown at different points



### Residual Stress Evolution

The evolution of residual stress was computed using temperature solution obtained at each time step. Figure 12(a) and (b) shows the corresponding quenching stresses developed after the solidification of the second and fourth layers, respectively. At the beginning of

solidification, deposited splats have near-zero stress values since they are in the molten state. However, during solidification, all solidified regions of the coating develop tensile quenching stress with a low magnitude of about 30 MPa. This low magnitude is attributed to the restriction of stress values with the use of the perfectly plastic material model. This is commonly done to consider stress relaxation



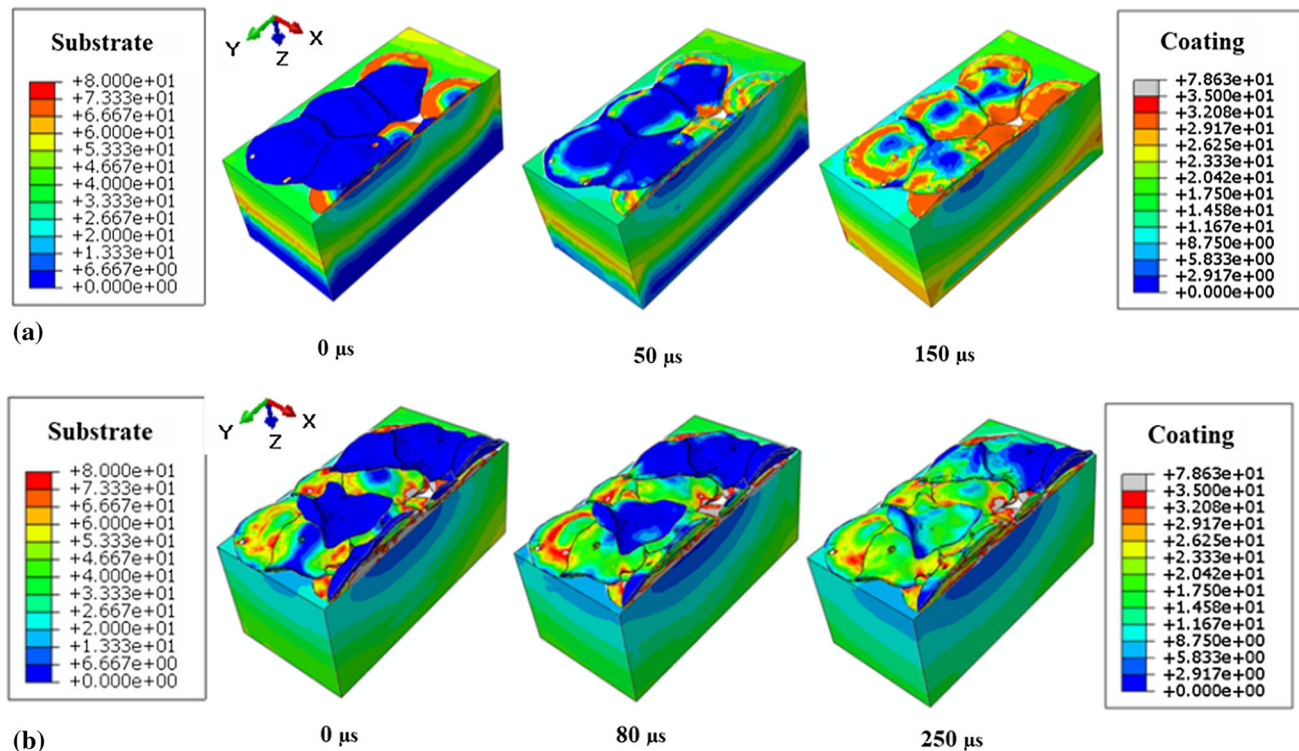


**Fig. 12** Evolution of quenching (von Mises) stress (MPa) during deposition of: (a) second and (b) fourth layers

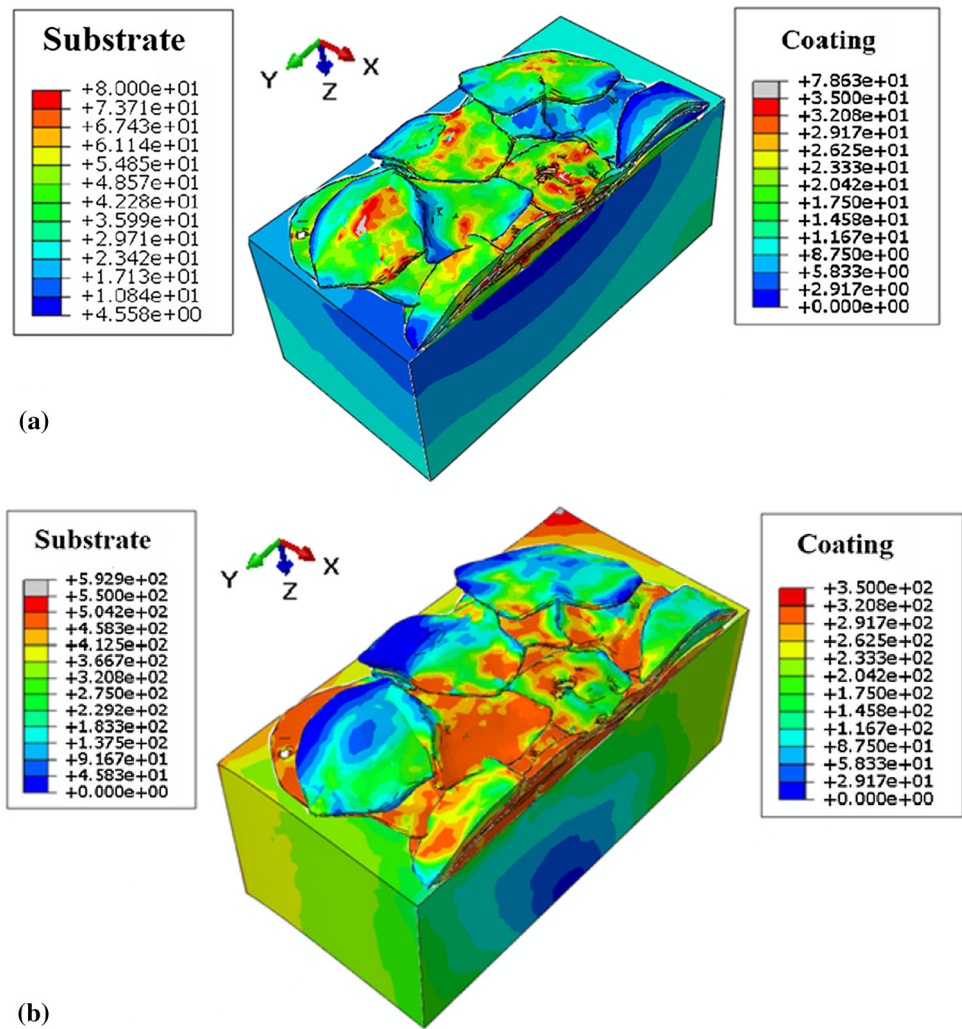
by microcracking and interfacial sliding within the ceramic coating layer [as found in previous works (Ref 6, 8, 46, 47)]. However, unlike with the previous models, quenching stresses predicted here display an uneven field distribution having a fluctuation of stress values because of process dependence and presence of discontinuities. Similar observations can be made with the fifth layer as demonstrated in Fig. 13(a). Moreover, the quenching stresses influence the final stress state of the coating layer despite its small magnitude. As demonstrated by Fig. 13(b), the von Mises residual stress field shows that very high residual stresses of about 300 MPa are developed at various critical regions within the coating microstructure. The residual stress field is dominated by post-deposition stresses due to the large difference in the coefficient of thermal expansions (CTEs) of coating and substrate layers.

For the analysis of results, the emphasis is given to in-plane normal stresses due to their significance on coating lifetime. Figure 14(a) and (b) shows the variation of biaxial in-plane deposition and residual stresses developed along the coating thickness. As observed in previous results by Buchmann et al. (Ref 42), the in-plane stresses (acting in  $x$ - and  $y$ -direction) are equi-biaxial, in the sense that they are almost equal in terms of both magnitudes despite acting in perpendicular directions. This has also been observed from the results of our hole drilling experiment (shown in

Fig. 15). The equi-biaxial nature of the stress profile is attributed to the nature of coating deposition. The coating is usually deposited in a layer-by-layer (or pass-by-pass) manner such that temperature gradient is more predominant along the thickness direction. However, as observed experimentally, minor differences occur between the two orthogonal stress profiles due to the presence of discontinuities (or imperfections) within the coating layer. Figure 14(a) and (b) shows that the quenching (deposition) stress developed after splat solidification is tensile with low values attributed to stress relaxation by microcracking and interfacial sliding as previously stated when discussing Fig. 12. Despite its low magnitude, the quenching stress influences the nature of the final residual stress profile, especially at the near-interface region of the coating layer.

It is well established in the literature (Ref 6) that ceramic coatings develop very high compressive post-deposition (mismatch) stress because of their low CTE as compared to the underlying substrate. Consequently, compressive residual stress is developed in the ceramic coating layer due to the dominance of mismatch (compressive) stresses over the low quenching (tensile) stresses. Thus, the residual stress profiles (shown in Fig. 14a and b) display equi-biaxial compressive stress values that increase with depth of coating layer. Also from the figures, it can also be seen that the residual stress profiles are fairly comparable to results obtained with Tsui and Clyne

**Fig. 13** von Mises stress field (MPa) developed in five-layer coating: (a) quenching stress and (b) residual stress



analytical model (Ref 5) for a coating layer deposited in 5 steps. The inputs to the analytical model were: elastic properties given in Table 1, intrinsic (quenching) stress of 30 MPa and same geometrical dimensions as used in numerical simulations. As an elastic material model with temperature-independent material properties was used to derive the analytical model, it is observed that deviation exists between the results obtained analytically and numerically especially at regions close to the interface. The analytical model overestimates the residual stress profile due to the assumptions made during derivation. Thus, for more realistic residual stress prediction, it is necessary to consider the nonlinear material behavior of the coating and substrate layers. For the ceramic coating layer, the presence of pores and microcracks considerable affects the residual stress profile. For metallic coatings, plastic deformation influences the stress profile more than pores and cracks. In all cases, it is essential to model the steel substrate layer with a robust material model that considers plastic deformation with proper strain hardening criterion. The high

compressive residual stress developed near the coating interface improves the adhesion strength of the coating layer. As found in previous studies (Ref 5, 8), Fig. 14(a) and (b) shows that the compressive residual stress developed within the coating layer is balanced by corresponding tensile stresses on the substrate side due to mismatch of structural properties at the coating–substrate interface. Specifically, Fig. 14 shows that the in-plane residual stresses developed at the interface (in  $x/y$  directions) are  $-110/-130$  MPa and  $310/370$  MPa on coating and substrate sides, respectively. The large difference between the stresses developed at the interface (in terms of magnitude and direction) signifies the influence of residual stresses on the adhesion strength/lifetime of coatings. The equi-biaxial compressive stresses (shown in Fig. 14) are comparable to the results of our hole drilling experiment and those of previous studies (Ref 5, 8, 42, 48, 49). As demonstrated in Fig. 15, the current numerical results fall within the expected range of stress values measured experimentally with incremental hole drilling method.

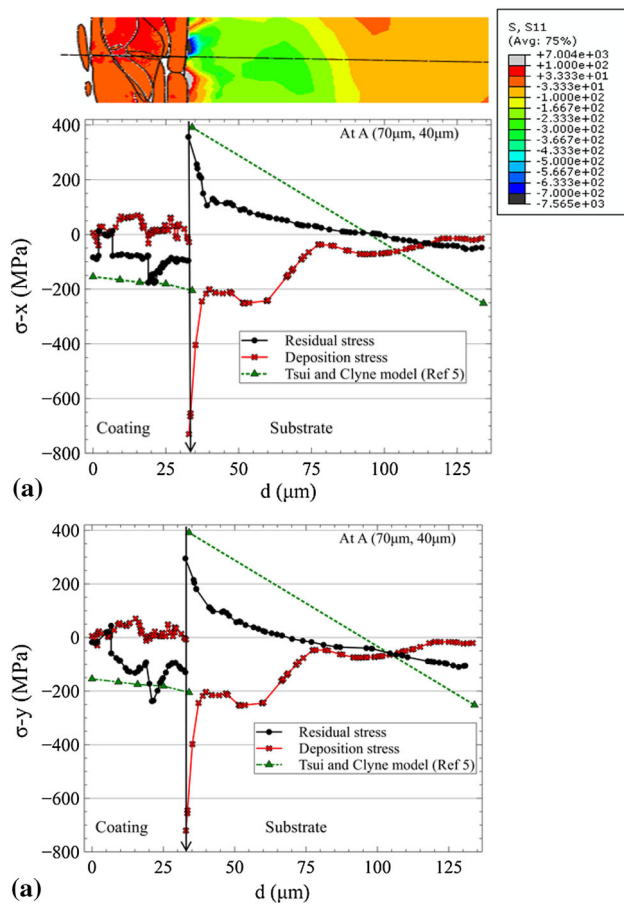


**Fig. 14** Biaxial in-plane stress profiles at A: (a) stress in  $x$ -direction and (b) stress in  $y$ -direction

Also, the overall trend of numerical and experimental stress profile is similar. As obtained numerically, the experimental results revealed that compressive residual stresses (which increase with depth) are developed within the ceramic coating layer. The substrate layer develops high tensile stresses, especially near the interface. Also, the nonlinear stress profile is developed due to the oscillation in strain readings caused by the presence of defects. The high compressive stresses measured experimentally near the coating surface are due to absurd variation in initial strain readings possibly caused by the high surface roughness or variable thickness of the coating layer.

Figure 16 shows the variation in other stress components along the thickness of the coating and substrate layers at point A. The normal (out-of-plane) residual stress acting in the  $z$ -direction is considerably high and tensile, especially at regions near the interface (as shown in Fig. 16a). The difference between the in-plane stresses developed at the interface on coating and substrate sides is small as compared to that of the equi-biaxial stresses explained previously. Consequently, the coating is weaker with loadings in  $z$ -direction than in other directions. As further

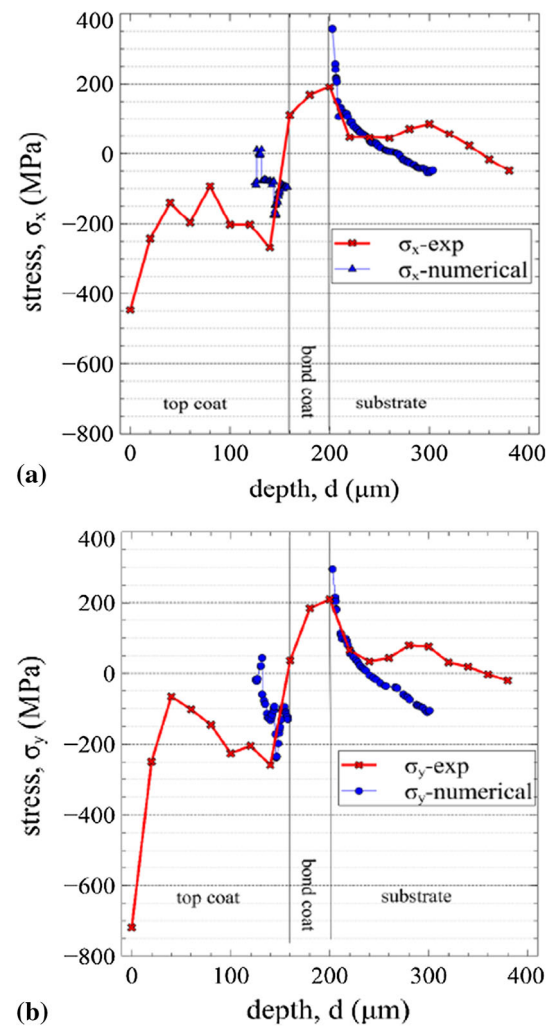


**Fig. 15** Comparison of residual stress profile (at A) with experimental results: (a) stress in  $x$ -direction and (b) stress in  $y$ -direction

confirmed by Fig. 16(b), it can be observed that the various stress components add up to result in higher von Mises stress variation along the coating thickness. The developed shear stresses are found to be very low with the  $xy$ -shear residual stress being the highest (shown in Fig. 16c). The maximum principal stress, shown in Fig. 16(d), seems qualitatively like the normal stress component in the  $z$ -direction. A similar observation is made at other locations. Figure 17(a) shows that, despite the low-temperature gradient along the width/length of the coating layer, there exists fluctuation of stresses to within same range of values due to obvious presence of discontinuities at random sites within the coating microstructure. The expansion and contraction of the substrate are tracked (at base) during splats solidification (i.e., second regime) and post-deposition cooldown (i.e., third regime), respectively (as shown in Fig. 17b). As expected, substrate expansion during splats solidification is not very significant due to



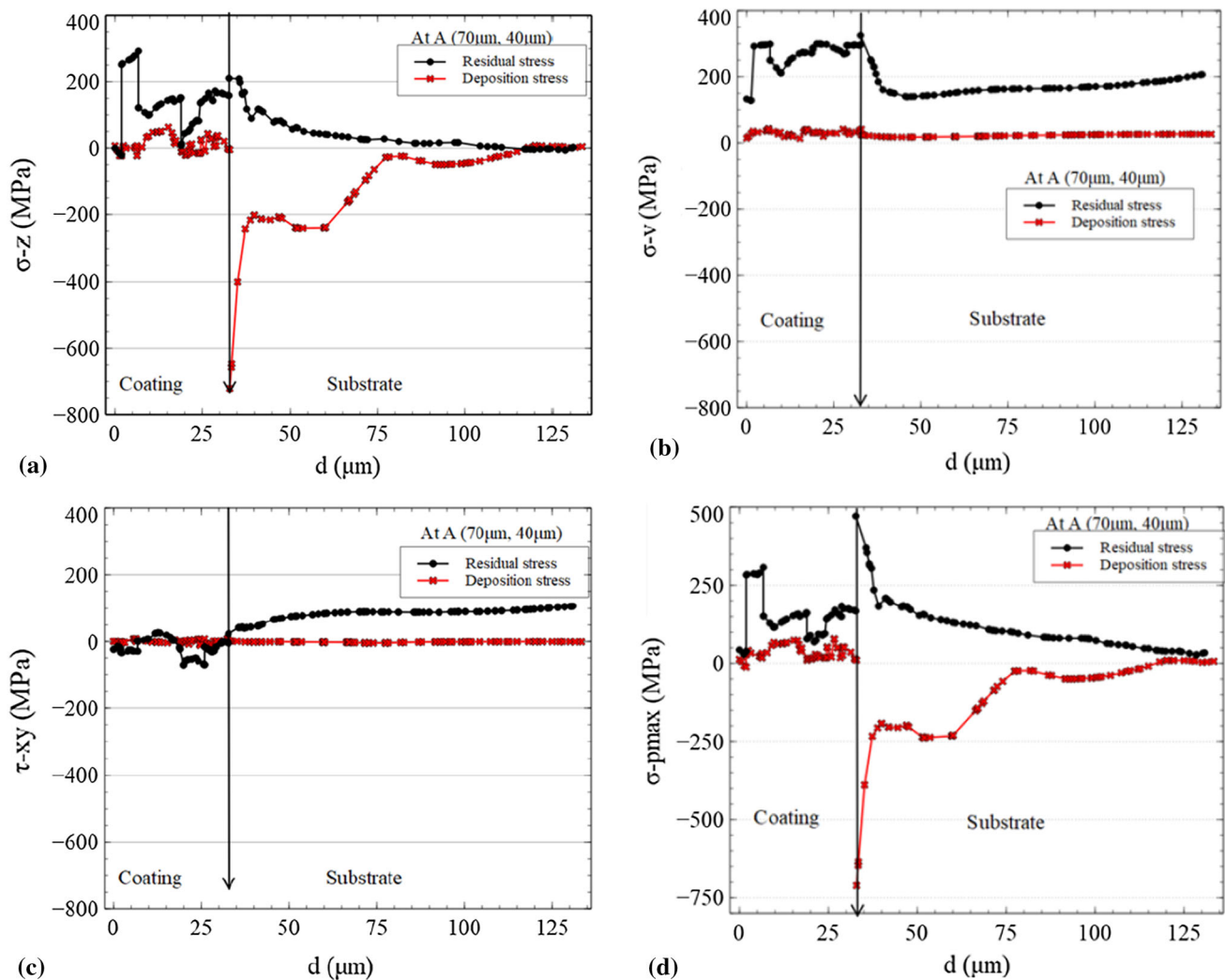


**Fig. 16** Other stress profiles at A: (a) in-plane normal stress, (b) von Mises stress, (c) shear stress and (d) maximum principal stress

localization of heat near the interface. However, during post-deposition cooldown stage, the substrate contracts considerably due to rapid decrease in temperature throughout the substrate layer.

## Conclusions

Residual stress is considered to have a significant influence on constitutive behavior, lifetime and integrity of thermal spray coatings including TBCs. Based on the results presented, the following conclusions can be made:

- The proposed hybrid approach has proven to be an efficient computational tool for the numerical prediction of residual stresses. Due to the large deformation associated with multiple droplets deposition, the

meshless methods (such as SPH) are found to be more suitable for the numerical modeling of the thermal spray process, while the evolution of temperature and residual stress in the multilayered coating are best modeled using grid-based numerical schemes (such as FEM) due to high stability.

- The results also show that the use of realistic process parameters leads to a more reliable estimation of residual stresses. As observed experimentally, we have predicted a residual stress profile that is nonlinear along the length and thickness of the coating. Specifically, it is found that the discontinuities such as pores and cracks lead to local stress relaxation in various regions within the coating layer. The relaxation of the residual stress field weakens several regions within the coating which can serve as a source of damage initiation while in active service.

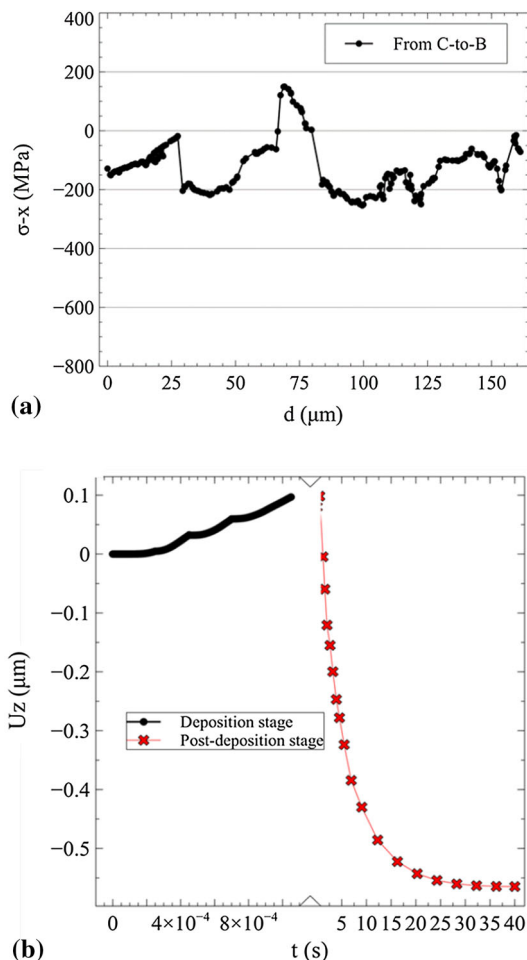


**Fig. 17** (a) Residual stress profile (acting in the  $x$ -direction) from C-to-B at 10  $\mu\text{m}$  above interface, (b) expansion/contraction of substrate layer (in positive  $z$ -direction) during deposition and post-deposition stages

**Acknowledgments** The authors would like to acknowledge the support provided by King Fahd University of Petroleum and Minerals (KFUPM) in funding this work through project FT161016.

## References

1. F. Hermanek, *Thermal Spray Terminology and Company Origins*, ASM International, Materials Park, 2001
2. R.B. Heimann, *Plasma-Spray Coating: Principles and Applications*, Wiley, New York, 2008
3. P. Araujo, D. Chicot, M. Staia, and J. Lesage, Residual Stresses and Adhesion of Thermal Spray Coatings, *Surf. Eng.*, 2005, **21**(1), p 35–40
4. Z. Xue, A.G. Evans, and J.W. Hutchinson, Delamination Susceptibility of Coatings Under High Thermal Flux, *J. Appl. Mech.*, 2009, **76**(4), p 041008
5. Y.C. Tsui and T.W. Clyne, An Analytical Model for Predicting Residual Stresses in Progressively Deposited Coatings Part 1: Planar Geometry, *Thin Solid Films*, 1997, **306**(1), p 23–33
6. A.A. Abubakar, A.F.M. Arif, K.S. Al-Athel, S.S. Akhtar, and J. Mostaghimi, Modeling Residual Stress Development in Thermal

- Spray Coatings: Current Status and Way Forward, *J. Therm. Spray Technol.*, 2017, **26**(6), p 1115–1145
7. L. Wang, Y. Wang, X.G. Sun, J.Q. He, Z.Y. Pan, and C.H. Wang, Finite Element Simulation of Residual Stress of Double-Ceramic-Layer  $\text{La}_2\text{Zr}_2\text{O}_7/8\text{YSZ}$  Thermal Barrier Coatings Using Birth and Death Element Technique, *Comput. Mater. Sci.*, 2012, **2012**(53), p 117–127
8. L. Wu, J. Zhu, and H. Xie, Numerical and Experimental Investigation of Residual Stress in Thermal Barrier Coatings During APS Process, *J. Therm. Spray Technol.*, 2014, **23**(4), p 653–665
9. M. Elhoriny, M. Wenzelburger, A. Killinger, and R. Gadow, Finite Element Simulation of Residual Stress Development in Thermally Sprayed Coatings, *J. Therm. Spray Technol.*, 2017, **26**(4), p 735–744
10. R. Berthelsen, D. Tomath, R. Denzer, and A. Menzel, Finite Element Simulation of Coating-Induced Heat Transfer: Application to Thermal Spraying Processes, *Meccanica*, 2016, **51**(2), p 291–307
11. B. Klusemann, R. Denzer, and B. Svendsen, Microstructure-Based Modeling of Residual Stresses in WC-12Co-Sprayed Coatings, *J. Therm. Spray Technol.*, 2011, **21**(1), p 96–107
12. J. Mostaghimi, S. Chandra, R. Ghafouri-Azar, and A. Dolatabadi, Modeling Thermal Spray Coating Processes: A Powerful Tool in Design and Optimization, *Surf. Coat. Technol.*, 2003, **2003**(163–164), p 1–11
13. C. Li, X. Zhang, Y. Chen, J. Carr, S. Jacques, J. Behnken, M. di Michiel, P. Xiao, and R. Cernik, Understanding the Residual Stress Distribution through the Thickness of Atmosphere Plasma Sprayed (APS) Thermal Barrier Coatings (TBCs) by High Energy Synchrotron XRD; Digital Image Correlation (DIC) and Image Based Modelling, *Acta Mater.*, 2017, **132**, p 1–12
14. M.Y. Zhang, H. Zhang, and L.L. Zheng, Simulation of Droplet Spreading, Splashing and Solidification Using Smoothed Particle Hydrodynamics Method, *Int. J. Heat Mass Transf.*, 2008, **51**(13), p 3410–3419
15. M. Zhang, Simulation of Surface Tension in 2D and 3D with Smoothed Particle Hydrodynamics Method, *J. Comput. Phys.*, 2010, **229**(19), p 7238–7259
16. A. Farokhpanah, J. Mostaghimi, and M. Bussmann, Free-Surface Enthalpy Method for Transient Convection/Diffusion Phase Change, *arXiv Prepr. arXiv1701.00463* (2017)
17. J.J. Monaghan, On the Problem of Penetration in Particle Methods, *J. Comput. Phys.*, 1989, **82**(1), p 1–15
18. M. Xue, S. Chandra, J. Mostaghimi, and C. Moreau, A Stochastic Coating Model to Predict the Microstructure of Plasma Sprayed Zirconia Coatings, *Model. Simul. Mater. Sci. Eng.*, 2008, **2008**(16), p 065006
19. N. Nayeibpashae, S.H. Seyedein, M.R. Aboutalebi, H. Sarpoolaky, and S.M.M. Hadavi, Finite Element Simulation of Residual Stress and Failure Mechanism in Plasma Sprayed Thermal Barrier Coatings Using Actual Microstructure as the Representative Volume, *Surf. Coat. Technol.*, 2016, **291**, p 103–114
20. M. Gupta, K. Skogsberg, and P. Nylén, Influence of Topcoat-Bondcoat Interface Roughness on Stresses and Lifetime in Thermal Barrier Coatings, *J. Therm. Spray Technol.*, 2014, **23**(1), p 170–181
21. Z. Zhu, S. Kamnis, and S. Gu, Numerical Study of Molten and Semi-Molten Ceramic Impingement by Using Coupled Eulerian and Lagrangian Method, *Acta Mater.*, 2015, **90**, p 77–87
22. J.W. Adams, R. Ruh, and K.S. Mazdiasni, Young's Modulus, Flexural Strength, and Fracture of Yttria-Stabilized Zirconia Versus Temperature, *J. Am. Ceram. Soc.*, 1997, **80**(4), p 903–908
23. H. Hayashi, T. Saitou, N. Maruyama, H. Inaba, K. Kawamura, and M. Mori, Thermal Expansion Coefficient of Yttria Stabilized



- Zirconia for Various Yttria Contents, *Solid State Ion*, 2005, **176**(5), p 613–619
24. F. Cervera, *Worldwide Guide to Equivalent Irons and Steels*, ASM international, Materials Park, 2006
  25. M. Zhang, H. Zhang, and L. Zheng, Application of Smoothed Particle Hydrodynamics Method to Free Surface and Solidification Problems, *Numer. Heat Transf. Part A Appl.*, 2007, **52**(4), p 299–314
  26. J.J. Monaghan, Smoothed Particle Hydrodynamics, *Annu. Rev. Astron. Astrophys.*, 1992, **30**, p 543–574
  27. S.D. Aziz and S. Chandra, Impact, Recoil and Splashing of Molten Metal Droplets, *Int. J. Heat Mass Transf.*, 2000, **43**(16), p 2841–2857
  28. M. Corsini, P. Cignoni, and R. Scopigno, Efficient and Flexible Sampling with Blue Noise Properties of Triangular Meshes, *IEEE Trans. Vis. Comput. Graph.*, 2012, **18**(6), p 914–924
  29. H. Edelsbrunner and E.P. Mücke, Three-Dimensional Alpha Shapes, *ACM Trans. Graph.*, 1994, **13**(1), p 43–72
  30. G. Kamberov, G. Kamberova, and A. Jain, in 3D Shape from Unorganized 3D Point Clouds BT: Advances in Visual Computing: First International Symposium, ISVC 2005, Lake Tahoe, NV, USA, 5–7 December 2005. Proceedings, ed. by G. Bebis, R. Boyle, D. Koracin, and B. Parvin (Springer, Berlin, 2005), pp. 621–629
  31. H. Hoppe, in Poisson Surface Reconstruction and Its Applications, *Proceedings of the 2008 ACM Symposium on Solid and Physical Modeling* (ACM, 2008), p. 10
  32. M. Kazhdan and H. Hoppe, Screened Poisson Surface Reconstruction, *ACM Trans. Graph.*, 2013, **32**(3), p 29
  33. M. Garland and Y. Zhou, Quadric-Based Simplification in Any Dimension, *ACM Trans. Graph.*, 2005, **24**(2), p 209–239
  34. S. Boyé, G. Guennebaud, and C. Schlick, Least Squares Subdivision Surfaces, *Comput. Graph. Forum*, 2010, **29**(7), 2021–2028. <https://doi.org/10.1111/j.1467-8659.2010.01788.x>
  35. ABAQUS, *ABAQUS Documentation*, Dassault Systèmes, Providence, 2013
  36. Oerlikon Metco, Nickel Chromium–Aluminum Thermal Spray Powders (2017), p. 1–4, [https://www.oerlikon.com/ecomaXL/files/metco/oerlikon\\_DSMTS-0091.5\\_NiCrAl.pdf&download=1](https://www.oerlikon.com/ecomaXL/files/metco/oerlikon_DSMTS-0091.5_NiCrAl.pdf&download=1). Accessed 20 Feb 2018
  37. Oerlikon Metco, 8% Yttria Stabilized Zirconia Agglomerated and HOSP Thermal Spray Powders (2017), pp. 1–6, [https://www.oerlikon.com/ecomaXL/files/metco/oerlikon\\_DSMTS-0001.10\\_8YO\\_ZrO\\_HOSP.pdf&download=1](https://www.oerlikon.com/ecomaXL/files/metco/oerlikon_DSMTS-0001.10_8YO_ZrO_HOSP.pdf&download=1). Accessed 20 Feb 2018
  38. Vishay-Micromeritics, Instruction Bulletin B-129-8: Surface Preparation for Strain Gage Bonding (2014), [http://www.vishaypg.com/docs/11129/11129\\_b1.pdf](http://www.vishaypg.com/docs/11129/11129_b1.pdf). Accessed 12 Mar 2018
  39. Vishay-Micromeritics, Instruction Bulletin B-127-14: Strain Gage Installations with M-Bond 200 Adhesive (2014), <http://www.vishaypg.com/doc?11129>. Accessed 12 Mar 2018
  40. T. Valente, C. Bartuli, M. Sebastiani, and A. Loreto, Implementation and Development of the Incremental Hole Drilling Method for the Measurement of Residual Stress in Thermal Spray Coatings, *J. Therm. Spray Technol.*, 2005, **14**(4), p 462–470
  41. M. Escibano and R. Gadow, in Residual Stress Measurement and Modeling for Ceramic Layer Composites, *27th International Cocoa Beach Conference on Advanced Ceramics and Composites: A ed. by W.M. Kriven and H.-T. Lin (USA, 2003)*, pp. 615–622
  42. M. Buchmann, R. Gadow, and J. Tabellion, Experimental and Numerical Residual Stress Analysis of Layer Coated Composites, *Mater. Sci. Eng. A*, 2000, **288**(2), p 154–159
  43. K. Berreth, M. Buchmann, R. Gadow, and J. Tabellion, in Evaluation of Residual Stresses in Thermal Sprayed Coatings, *Proceedings of International Thermal Spray Conference, Düsseldorf* (1999)
  44. M. Vardelle, A. Vardelle, A.C. Leger, P. Fauchais, and D. Gobin, Influence of Particle Parameters at Impact on Splat Formation and Solidification in Plasma Spraying Processes, *J. Therm. Spray Technol.*, 1995, **4**(1), p 50–58
  45. S. Alavi and M. Passandideh-Fard, Numerical Simulation of Droplet Impact and Solidification Including Thermal Shrinkage in a Thermal Spray Process, *Front. Heat Mass Transf.*, 2011, **2**, p 023007
  46. J. Matejcek and S. Sampath, In Situ Measurement of Residual Stresses and Elastic Moduli in Thermal Sprayed Coatings Part 1: Apparatus and Analysis, *Acta Mater.*, 2003, **51**(3), p 863–872
  47. S. Kuroda, T. Dendo, and S. Kitahara, Quenching Stress in Plasma Sprayed Coatings and Its Correlation with the Deposit Microstructure, *J. Therm. Spray Technol.*, 1995, **4**(1), p 75–84
  48. H. Liu, F. Azarmi, M. Bussmann, J. Mostaghimi, and T.W. Coyle, Experiments and Simulation of Rapid Solidification of Air Plasma Sprayed Alloy 625 on Stainless Steel, *Surf. Coat. Technol.*, 2010, **204**(9–10), p 1521–1527
  49. J. Liu, R. Bolot, and S. Costil, Residual Stresses and Final Deformation of an Alumina Coating: Modeling and Measurement, *Surf. Coat. Technol.*, 2015, **2014**(268), p 241–246